AIAA JOURNAL
Vol. 47, No. 11, November 2009

Molecular Tagging Using Vibrationally Excited Nitric Oxide in an Underexpanded Jet Flowfield

Andrea G. Hsu,* Ravi Srinivasan,† Rodney D. W. Bowersox,‡ and Simon W. North§
Texas A&M University, College Station, Texas 77843

DOI: 10.2514/1.39998

We report a laser diagnostic technique which relies on planar laser-induced fluorescence of vibrationally excited nitric oxide ($NO_{v=1}$) molecules produced from the 355 nm photodissociation of seeded NO_2 for molecular tagging velocimetry applications. The technique was applied toward an axisymmetric highly underexpanded jet flowfield to yield single-component (streamwise) velocity maps. Detection of the photodissociated $NO_{v=1}$ molecules would be valuable in flow environments where molecular tagging velocimetry would be highly desirable, but where there are also significant background concentrations of NO. The technique would also be valuable in high-quenching and/or low-velocity flow conditions due to the long-lived nature of the photodissociated NO molecules. Single-shot streamwise velocity uncertainties were about 5% and could be lowered by increasing signal to noise. In addition, the vibrational relaxation of NO was explored in support of a U.S. Air Force Office of Scientific Research Multidisciplinary University Research Initiative project and it was found that the vibrational decay of NO was heavily dependent on collisional vibrational relaxation with oxygen atom formed through NO_2 photodissociation.

Nomenclature

C_{12}	=	experimentally determined calibration constant
D_e	=	nozzle diameter
D_m	=	Mach disk diameter
k	=	Boltzmann constant
P_a	=	ambient pressure
P_e	=	exit pressure
P_o	=	stagnation pressure
S_f	=	fluorescence signal intensity
T_o	=	stagnation temperature
T_{vib}	=	vibrational temperature
w	=	primary wavelength
X_m	=	distance from nozzle to Mach disk
$\Delta E_{21\text{vib}}$	=	energy difference between vibrational states

I. Introduction

VELOCITY is a very important parameter in the characterization of aerodynamic flowfields. There are two approaches used to measure velocity: probe-based (intrusive) and laser-based (nonintrusive) techniques. Two widely used nonintrusive techniques relevant to this study are particle image velocimetry (PIV) and molecular tagging velocimetry (MTV). PIV and MTV are planar techniques and can therefore provide instantaneous two-component velocity maps. Both MTV and PIV require a pair of images: an initial image and a time-delayed image. The velocity is calculated by dividing the spatial displacement by the known temporal separation between the two images. PIV diagnostics require the use of seeded particles, and although these particles are small (<1 μm), they often cannot follow the flow as precisely as molecules, particularly in the region of strong shocks, as shown in [1]. In addition, the seeding of particles is undesirable in some facilities, where the particles may clog the facility, coat optical windows, or cause damage by impinging on surfaces. MTV relies on the tagging of molecules by a "write" laser pulse, which are subsequently probed at a known time delay by a "read" laser pulse. MTV encompasses a wide range of techniques that can be applied in both gaseous and liquid flowfields and includes both line and gridded variants. Line MTV provides a single component of velocity by observing the spatial displacement of the line, whereas gridded techniques provide two components of velocity in the laser plane by observing the warping of the grid, that is, the spatial displacement of the grid intersection points. Several examples of gaseous MTV techniques are ozone tagging velocimetry (OTV), hydroxyl tagging velocimetry (HTV), Raman excitation plus laser-induced electronic fluorescence (RELIEF), nitric oxide (NO) tagging velocimetry, and NO_2 photodissociation. OTV involves the photolytic formation of ozone, which is then photodissociated to form vibrationally hot O_2 and simultaneously probed via Schumann–Runge fluorescence, as in [2]. HTV involves the photodissociation of water and followed by detection of OH by laser-induced fluorescence (LIF) [3–5]. RELIEF involves LIF probing of tagged vibrationally excited O_2 molecules, as in [6]. NO tagging velocimetry is conducted using naturally occurring NO, as in [7], by photodissociation of air [8,9], or by photodissociation of NO_2 [10,11]. In all three cases, reported studies have been limited to probing of the ground vibrational state of NO ($NO_{v=0}$) at 226 nm.

Studies in [7] have used NO tagging velocimetry where a write laser beam is used to electronically excite a line of naturally occurring NO in a hypersonic shock tube flowfield. The tagged NO decays with its fluorescence lifetime. Shortly after excitation, the tagged NO is read by imaging its fluorescence onto a short-exposure intensified charge-coupled device (ICCD) camera. A second image is obtained at a later time when the flow has experienced some spatial displacement. Based on the spatial displacement of the NO molecules, the streamwise velocity can be extracted from the data. This single laser experiment relies on conditions where the flow velocities must be sufficiently large so that the tagged NO undergoes reasonable spatial displacement within its fluorescence lifetime. In environments characterized by either low velocities or high fluorescence quenching, the time delays required for adequate spatial displacement exceed the fluorescence lifetime, decreasing signal to noise in the second image obtained and limiting the application of the technique. An alternative is the use of NO_2 photodissociation [10,11]. Instead of probing NO, which is dispersed throughout the flow, the photodissociation of NO_2 writes a column of spatially localized NO (and O atom) where the NO itself serves as the "tagged" molecules. The NO is then read at two subsequent times by two separate laser pulses via

Presented as Paper 1447 at the 47th AIAA Aerospace Sciences Meeting, including The New Horizons Forum and Aerospace Exposition, Orlando, FL, 5–8 January 2009; received 23 July 2008; revision received 10 July 2009; accepted for publication 18 July 2009.

*Chemistry Department. Member AIAA.
†Aerospace Engineering Department. Member AIAA.
‡Aerospace Engineering Department. Associate Fellow AIAA.
§Chemistry Department.

electronic excitation followed by fluorescence imaging. However, because the NO itself serves as the tag, the images need not be obtained during a single fluorescence lifetime. NO is also chemically stable and its depletion is only dependent on fluid mixing and diffusion. Thus, the photogenerated NO can be tracked on a timescale considerably longer (micro- to milliseconds) than excited state fluorescence (~10–200 ns depending on quenching conditions). In this paper, the write laser refers to the photodissociation laser, and the read lasers refer to the NO fluorescence probe lasers.

In addition, the photodissociation of NO_2 at 355 nm produces both ground and excited vibrational states of NO as shown by the following equation:

$$\begin{aligned} NO_2 + hv_{355\ nm} &\rightarrow NO_{v=0} + O \\ &\rightarrow NO_{v=1} + O \end{aligned} \tag{1}$$

with an experimentally determined branching ratio of $NO_{v=1}$:$NO_{v=0}$ of 41.2 ± 6.2:58.8 ± 8.8 as discussed in [12–14]. This branching ratio is well known and corresponds to a two-level Boltzmann vibrational temperature of 6700 K. In flow environments where there are significant background concentrations of NO, probing $NO_{v=1}$ rather than $NO_{v=0}$ can provide a significant signal-to-noise enhancement if background NO exists primarily in the ground vibrational state. Examples of such environments include high enthalpy facilities, combustion systems, and nonequilibrium air plasma flows.

The present study also includes an explanation of the mechanisms of the NO vibrational temperature decay as a function of space and time. This study is motivated by the recent increased interest in characterization of thermal nonequilibrium systems, such as those discussed in [15–19]. These systems are often encountered in hypersonic flowfields, where vibrational temperatures can reach thousands of Kelvin, trapping significant energy in molecular vibration. As a component of a U.S. Air Force Office of Scientific Research (AFOSR) sponsored Multidisciplinary University Research Initiative (MURI) program, we have been investigating the coupling of molecular nonthermal equilibrium (NTE) and turbulence. The term NTE refers to a state in which the molecules are in thermal nonequilibrium. Because the dissipation of turbulent kinetic energy is a collision-driven process, molecular nonequilibrium may significantly alter the basic turbulence energy budget dynamics. The experimental goals include providing quantitative measurements of the key second-order moments in canonical flows with and without molecular nonequilibrium and the advancement of laser diagnostic capabilities for multiparameter fluctuating turbulence measurements in nonequilibrium flows. In those experiments, a capacitively coupled radio frequency (CCRF) plasma is employed to produce vibrational NTE in low-temperature ($T_{rot} \sim T_{trans} \sim 300$ K) flowfields to assess the influence of vibrational relaxation. We find that the photodissociation of NO_2 provides a clean source of vibrationally excited NO with little rotational and translational excitation and is therefore a convenient system by which to calibrate planar laser-induced fluorescence (PLIF) diagnostics of NO vibrational thermometry in NTE flowfields characterized by 300 K rotational and translational temperatures and vibrational temperatures in excess of 2000 K. In addition, comparing experimental vibrational decays of NO to modeling can serve to validate vibrational kinetics modeling for further understanding of the driving mechanisms for NO vibrational decay. In addition, this technique would be useful in environments where the presence of water vapor or O_2 is undesirable, where OTV and HTV cannot be applied. The technique has also been applied toward combustion diagnostics, as demonstrated in [20], although in such environments, the decomposition of NO_2 must be considered and NO_2 must be preseeded (as naturally occurring NO_2 levels would be too low to support this diagnostic technique).

The NO vibrational temperature can be imaged by probing the populations of the two vibrational levels of NO simultaneously using NO PLIF as shown in [21]. Therefore, the vibrational temperature decay of NO can be temporally tracked. The fluorescence signal intensity is a complicated function of the initial population of the probed state, the ratio of the stimulated emission Einstein coefficients, the saturation and laser intensities, the spontaneous emission Einstein coefficient, and an overall efficiency term which can be obtained via a calibration point as shown in [22]. However, the ratio of two fluorescence signals that are obtained in the linear fluorescence regime by probing identical rotational states and two different vibrational levels cancels out many of these variables and yields a simple equation where the vibrational temperature can be directly calculated, as shown next. The quenching rates in the excited electronic state (A state) are also nearly equal for the ground ($v = 0$) and excited vibrational level ($v = 1$) as shown in [23]. Further details on the derivation of this equation and its validity for NO PLIF can be found in [21]:

$$R = \frac{S_{f2}}{S_{f1}} = C_{12} e^{\frac{-\Delta E_{21vib}}{kT_{vib}}} \tag{2}$$

Then, by imaging the NO fluorescence onto ICCD sensors, a vibrational temperature map can be determined by performing pixel-by-pixel calculation of the vibrational temperature.

We demonstrate both the velocimetry and vibrational temperature studies in a highly underexpanded, axisymmetric free jet flowfield. The terminology that will be used in this study was referenced from [24]. Briefly, underexpanded jets are broken down into two categories: moderately underexpanded and highly underexpanded jets. Moderately underexpanded jets possess a shock diamond structure caused by oblique shock waves, whereas highly underexpanded jets possess a Mach disk. The transition from subsonic to moderately underexpanded to highly underexpanded is a function of the jet pressure ratio (JPR), which is defined as the ratio of the exit pressure to ambient pressure P_e/P_a. Generally, jets with JPRs > 2 are defined as highly underexpanded. The structure of the highly underexpanded jet is well known [25] and relevant structures to this study are labeled in Fig. 1. At the nozzle exit, Prandtl–Meyer expansion fans give rise to the barrel shock structure that surrounds the inner isentropic expansion region. The expansion in this region is terminated by a Mach disk which recompresses the flow. The intersection of the barrel shock and Mach disk is known as the Mach disk triple point and this point gives rise to a slip line between the subsonic core (inner jet) and supersonic region (outer jet) which develops into a shear layer. There also exists a shear layer between the outer jet and ambient, nearly stagnant, fluid. As the fluid travels past the plane of the Mach disk, a series of oblique shocks recompress the flow, but there are no further normal shocks for very highly underexpanded jets [25]. These oblique shocks cause weak oscillations in the streamwise velocity and temperature.

The structure of underexpanded jets is usually classified by distance to Mach disk X_m, diameter of Mach disk D_m, and primary wavelength w which have all been found to be a function of the JPR [26]. Underexpanded jets can be further classified as laminar, transitional, and turbulent underexpanded jets by defining a Reynolds number that takes into account the JPR [27]. Transition is caused by instabilities within the shear layer that develop between the inner and outer regions, giving rise to fluid mixing between these two regions as the flow becomes more and more turbulent. By using this

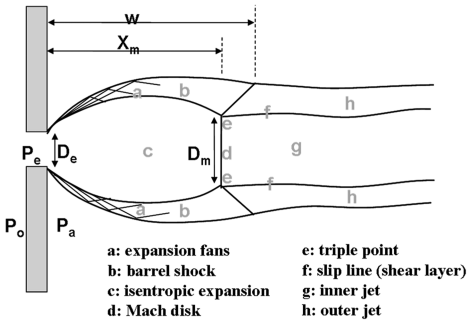

Fig. 1 Relevant structures associated with a highly underexpanded jet flowfield.

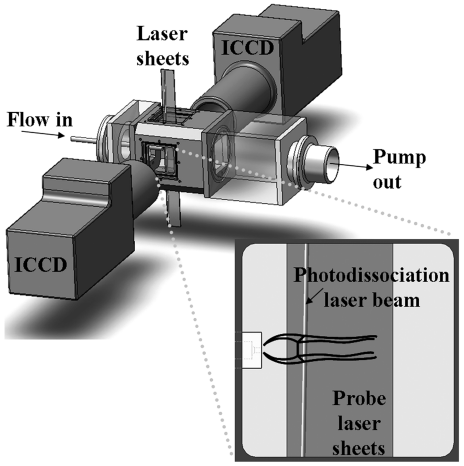

Fig. 2 Schematic of experiment and close up of field of view.

Reynolds number, the distance from the nozzle exit to transition and also to turbulence can be calculated as in [27]. Recent studies of the underexpanded jet have focused on measurements of simultaneous temperature and velocity using NO PLIF [28], simultaneous pressure and temperature measurements using N_2 coherent anti-Stokes Raman spectroscopy [24], and simultaneous pressure, velocity, and temperature measurements using high spectral resolution NO PLIF as in [29]. Numerical studies have focused primarily on a comparison of the measured properties of underexpanded jet structure with computational fluid dynamics as in [26].

The present experiment represents the first known use of probing $NO_{v=1}$ (rather than $NO_{v=0}$) via the NO_2 photodissociation MTV technique toward single-component velocity mapping. We anticipate that the technique will be valuable in flowfields with high fluorescence quenching, large ambient NO background, or low velocities where NO fluorescence lifetime is not adequate for obtaining sufficient spatial displacement. In addition, a study into the vibrational decay of NO motivated by an AFOSR MURI program will be briefly included.

II. Experimental Setup

A. Single-Component Molecular Tagging Velocimetry

The experiments were conducted in a vacuum chamber which was fitted with a nozzle to create the highly underexpanded jet flowfield. The nozzle construction was simple, and consisted of $\frac{1}{4}$ in. stainless steel sealed tubing with a 1-mm-diam circular nozzle throat. The chamber was continuously evacuated (pumping speed $\sim$250 cfm) to maintain steady ambient pressures using a roots blower and backing pump. Optical access was available via quartz windows on four - sides. The stagnation and ambient pressures were monitored using calibrated pressure transducers (MKS Series 902). The N_2 was high-purity gas from Brazos Valley Welding, and the NO_2 was supplied by Sigma Aldrich (>99.5% pure). The NO was diluted using N_2 from a 10% NO/N_2 mix, supplied by Matheson Tri-Gas. The overall timing for the entire experiment was controlled by a digital delay generator (Berkeley Nucleonics Corporation, model DG565). Figure 2 shows the schematic layout of the setup with a close up of the field of view.

The timings for the laser pulses are as follows. The photodissociation laser (Spectraphysics PRO 290-10, 355 nm at 10 Hz) was focused into a beam and generated a column of local thermal nonequilibrium distribution of $NO_{v=1}$ and $NO_{v=0}$. The NO probe laser systems consisted of two frequency doubled Sirah Cobrastretch dye lasers pumped by two Spectraphysics LAB 150-10 Nd:YAG lasers operating at 10 Hz and 355 nm to produce tunable UV laser light at around 224–226 nm. At 100 ns after photodissociation, the first probe laser sheet read the initial location of $NO_{v=1}$ molecules by fluorescence imaging onto an ICCD camera (Andor iStar ICCD, model DH734, 16 bit, fitted with a Nikon 105 mm F/4.5 UV lens). No filters were used to maximize the transmitted fluorescence signal, and elastic scatter was temporally minimized by delaying the cameras approximately 10 ns after the arrival of the probe laser pulse. The second image was taken 500 ns after photodissociation by a second probe laser and ICCD camera, also imaging $NO_{v=1}$. The camera gates were set at 50 ns. Because the camera gate width is not negligible compared to the temporal delay between images (400 ns), systematic errors in the velocimetry calculation were accounted for using the timing calculations described in [7]. The measured NO displacement was divided by the known time delay to give the streamwise velocity. The NO rotational states probed for the first and second probe lasers were $R_1 + Q_{21}(1.5)$ and the group of lines which form the bandhead surrounding $Q_1(1.5)$, respectively, in the $A^2\Sigma^+_{1/2}(v' = 1) \leftarrow X^2\Pi_{1/2}(v'' = 1)$ transition. These lines were chosen because they are well populated over the temperature range (20–300 K) expected in the underexpanded jet flowfield. To demonstrate the advantages of probing $NO_{v=1}$ over $NO_{v=0}$, the experiment was repeated, except $NO_{v=0}$ was probed instead of $NO_{v=1}$. The rotational states of $NO_{v=0}$ probed were $R_1 + Q_{21}(2.5)$ for both probe lasers in the $A^2\Sigma^+_{1/2}(v' = 0) \leftarrow X^2\Pi_{1/2}(v'' = 0)$ transition. The probed rotational states for both $NO_{v=1}$ and $NO_{v=0}$ were located using the spectral simulation software LIFbase [30]. The power of the photodissociation beam was approximately 10 mJ/pulse at the test section, and the calculated NO_2 photodissociation fraction was greater than 99.9%. The short temporal separation (400 ns) between the initial and time-delayed image was used for increased spatial resolution. The experimental conditions are listed in Table 1. Further detail on the experimental setup and timings are provided in [31].

The experiments were carried out using both integrated (30 s) and single-shot images. All images were obtained at full resolution (1024×1024 pixels). The photodissociation beam was formed by blocking the laser using a pair of facing razor blades just before its entrance into the vacuum chamber. The width of the beam was approximately 700 μm. The integrated images were taken by translating the razor blade assembly, starting from the nozzle across the flowfield to past the Mach disk and taking initial and time-delayed images at each location. Sixteen total locations were used. A statistical set of single-shot images (630 images) at location 7 of 16 were taken for uncertainty analyses. Sample raw images of the experiments probing $NO_{v=0}$ and $NO_{v=1}$ are shown in Figs. 3 and 4, respectively. The field of view is about 14×14 mm. Each of the locations were approximately equidistant, so that adjacent lines were approximately 800 μm apart. Simply from visual assessment of the raw images, it is clear that the images probing $NO_{v=0}$ suffer from background NO fluorescence. The photodissociated NO is clear in both cases, although the $NO_{v=1}$ images provide much larger contrast and hence better signal to noise.

B. Nitric Oxide Vibrational Temperature Decay

As part of an AFOSR-funded MURI project, the NO vibrational temperature decay was measured using long time delays (μs steps). The goal was to create a local-nonthermoequilibrium distribution of NO molecules and then map out the vibrational energy decay of NO

Table 1 Molecular tagging velocimetry experimental conditions

					Mole Fraction			
Probed state	P_a, torr	P_0, torr	JPR	T_o, K	NO	N_2	NO_2	O_2
$NO_{v=0}$	4.8	450	49.53	300	0.009	0.921	0.07	0.00
$NO_{v=1}$	4.6	450	51.68	300	0.02	0.94	0.04	0.00

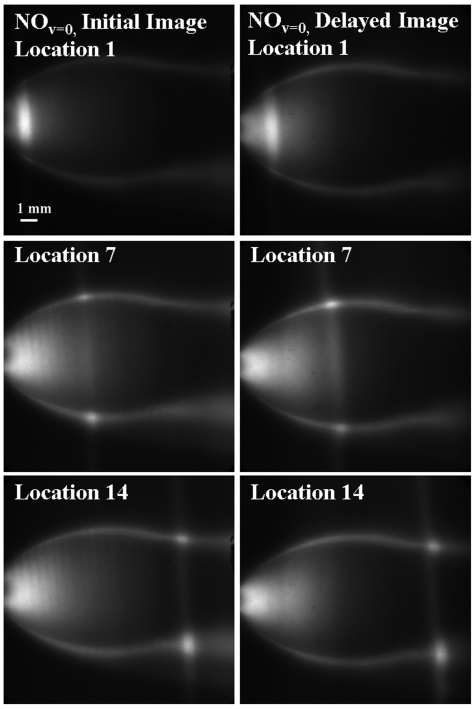

Fig. 3 Initial and time-delayed integrated images for molecular tagging velocimetry studies, probing $NO_{v=0}$.

as a function of space and time in the flowfield. The experiment was valuable for validating the vibrational kinetics modeling to describe the vibrational energy exchange and decay between flow species following the CCRF discharge. This experiment was first conducted in a simple static cell and then was conducted in the underexpanded jet flowfield because the underexpanded jet flowfield offered a variety of pressure and temperature conditions in one simultaneous flowfield, which could be used in comparison to vibrational kinetics modeling. The results presented in this paper pertain to the underexpanded jet flowfield. The experimental conditions are as follows:

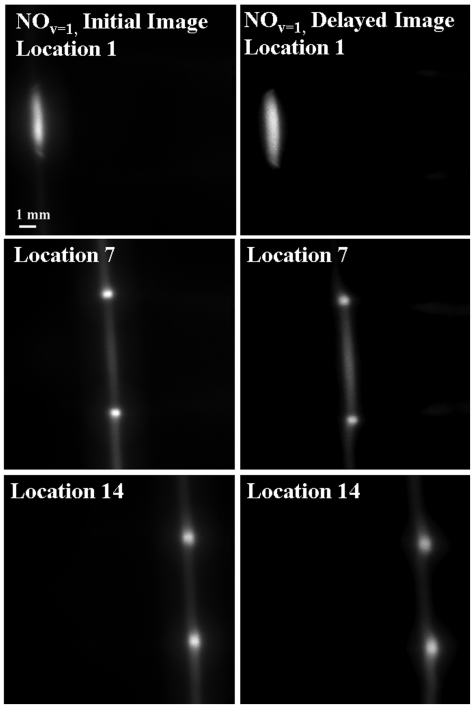

Fig. 4 Initial and time-delayed integrated images for molecular tagging velocimetry studies, probing $NO_{v=1}$.

$P_a = 12.3$ torr, $P_0 = 551.8$ torr, JPR = 23.70, $T_o = 300$ K, bulk gas (air) mole fraction = 0.976, NO_2 mole fraction = 0.024, and $Re = 1.67 \times 10^6$ m^{-1}.

The timing for this experiment was different than that of the velocimetry experiment. At some time delay $t1$ after photodissociation, the $NO_{v=1}$ was probed by the first probe laser. A short time after the $NO_{v=1}$ probe laser pulse $t2$, $NO_{v=0}$ was probed by the second probe laser. The probe laser powers (1–2 m J/pulse) were experimentally verified to be in the linear fluorescence regime. However, it should be noted that saturation of the fluorescence signal would be desirable because the fluorescence signal would be independent of laser power. Such laser powers (18–20 m J/pulse) are currently possible with optical parametric oscillator and sum-frequency mixing schemes.

The temporal separation between the $NO_{v=1}$ and $NO_{v=0}$ probe lasers ($t2$, which was 150 ns) was not changed. However, the time delay after photodissociation ($t1$) was changed in steps of μs. In this way, a vibrational temperature map at each $t1$ could be produced through the use of Eq. (2), and the collection of maps as a function of $t1$ results in a NO vibrational temperature decay. In this experiment, NO rotational states $R_1 + Q_{21}(3.5)$ were used for both $NO_{v=1}$ and $NO_{v=0}$. These rotational states were chosen because they would be well populated in the low temperatures expected in the underexpanded jet flowfield and were well separated from other rotational lines. The photodissociation laser beam was positioned in the postshock region of the highly underexpanded jet, just beyond the Mach disk. The main reason for this choice was that, in the cold expansion region before the Mach disk, the vibrational temperature would freeze out and so would not be adequate for demonstrating vibrational relaxation. For this experiment, the ICCD cameras were binned 2×2 for a final image size of 512×512 pixels and mapped to a field of view of 18.4×18.4 mm^2. Figure 5 shows the location of the nascent NO molecules in relation to the highly underexpanded jet flowfield at nominal delays of 0 and 12 μs. The images were constructed by overlaying images of the raw molecular tagging data with 1% NO in N_2 run at the same JPR as the molecular tagging data. We interrogated specific regions of the flow due to the differing pressures, and thus different decay rates. The interrogated areas were the ambient region, centerline region, and the turbulent outer jet regions, which are labeled in the right panel of Fig. 5. The scaled Reynolds number was calculated using expressions found in [27].

Data were acquired at various nominal time delays from 0 to 200 μs and consisted of 62 image pairs. In addition, 40 single-shot images at each of the time delays (0, 5, 10, 15, 20, 25, and 30 μs) were taken for statistical error analyses. Sample raw (uncorrected) images of $NO_{v=0}$ and $NO_{v=1}$ are shown in Fig. 6. The vibrational decay is qualitatively apparent through comparison of the $NO_{v=0}$ and $NO_{v=1}$ images because the $NO_{v=1}$ images have a much more rapid relative decay than the $NO_{v=0}$ images.

III. Results and Analysis

The important difference between the two studies was that the molecular tagging velocimetry study was focused on time-correlated velocimetry using a short time delay (few hundred nanoseconds)

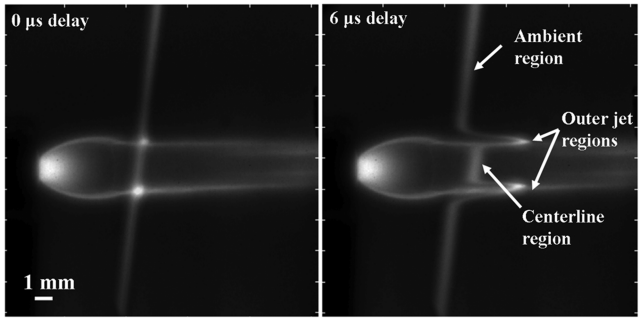

Fig. 5 Highly underexpanded jet flowfield: JPR = 23.7, $Re = 1.67 \times 10^6$ m^{-1}, 2.4% NO_2 in dry air for vibrational temperature study.

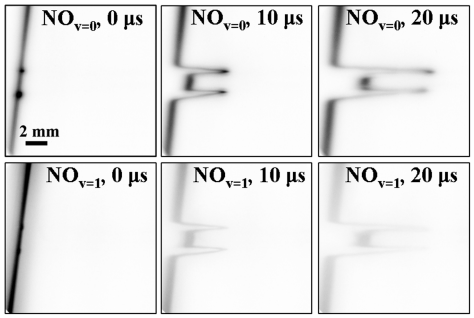

Fig. 6 Raw images of 0, 10, and 20 μs for the $NO_{v=0}$ (top) and $NO_{v=1}$ (bottom) probe lasers for vibrational temperature study.

between the image pairs for better spatial resolution. Therefore, each pair of single-shot images represents an instantaneous velocity measurement. Vibrational temperature is not addressed in this experiment because the short time delay is inadequate for vibrational energy decay which occurs on the μs timescale. The main objectives of the molecular tagging velocimetry study are 1) to show the advantages of probing $NO_{v=1}$ over $NO_{v=0}$ for single-component velocimetry for suppressing the effects of background NO fluorescence, and 2) to demonstrate the use of photodissociation of NO_2 and probing of $NO_{v=1}$ for low uncertainty single-component velocimetry through single-shot image analyses.

The NO vibrational temperature decay study focused on time-correlated vibrational temperature analysis using long time delays (tens of microseconds) in support of an AFOSR-funded MURI project. In this case, because the images at long time delays suffered from low signal to noise, velocimetry accuracy was reduced and was not the focus of the study. Rather, the main objective of the NO vibrational temperature decay study were 1) to map the vibrational temperature decay of NO molecules as a function of time and space, and 2) to explore the underlying chemical kinetics mechanisms which control the vibrational decay of NO. The results from both the velocimetry and vibrational temperature studies are presented here.

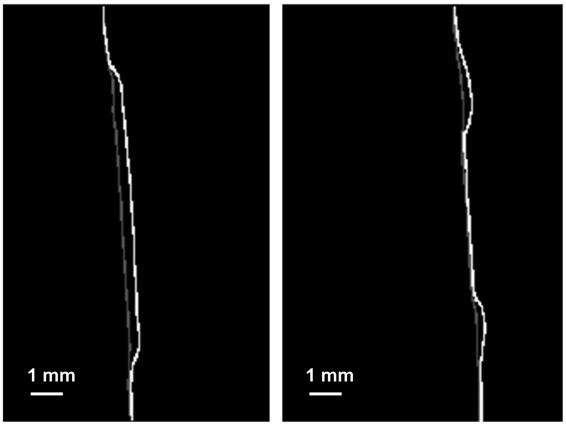

Fig. 7 Spatial displacement at locations before (left) and after (right) the Mach disk for velocimetry study.

A. Integrated and Single-Shot Images for Single-Component Velocimetry

The integrated image pairs for each photodissociation line position were analyzed separately and added to generate a streamwise velocity map. Edge-finding procedures were used to locate the rising and falling edges of each photodissociation line, and the streamwise spatial displacement of the edges were tracked and divided by the temporal separation (400 ns) to calculate the streamwise velocity. Sample images are shown in Fig. 7. The left image corresponds to a location about two-thirds of the way from the nozzle to the Mach disk within the expansion region, and the right image corresponds to a location nearly immediately after the Mach disk. The gray line is the initial position, whereas the white line is the 400-ns-delayed location. It is evident from the images that, in the left panel, the gas is moving rather uniformly in the streamwise direction in the expansion region; in the right panel, the subsonic core is shown by smaller streamwise spatial displacement, and is framed on top and bottom by the supersonic outer jets depicted by larger spatial displacements.

To calculate the velocity, the software located each edge in the initial image and then searched for the corresponding edge in the delayed image using a user-defined pixel roaming value. Because two edges are located for each photodissociation line at each location, two streamwise velocity profiles were calculated. This process was repeated for each image pair. The resulting streamwise velocity lines were added together to create a velocity map, as shown in Fig. 8. The images were smoothed using a standard Gaussian spatial filter, producing a final resolution of 500×500 μm in the field of view. The derived velocity map exhibits structures consistent with the underexpanded jet. In the streamwise direction, the flow accelerates to hypersonic velocities until it reaches the Mach disk, where the flow experiences a normal shock resulting in subsonic speeds. After the Mach disk, the supersonic outer jet regions and subsonic core are clearly identified in the velocity map (Fig. 8) as well.

To characterize the measurements' uncertainty, 630 single-shot images were taken at location 7 which was located roughly two-thirds of the distance from the nozzle to the Mach disk in the expansion region. The single-shot interpolated velocity maps were averaged to produce an average streamwise velocity map. The spatial

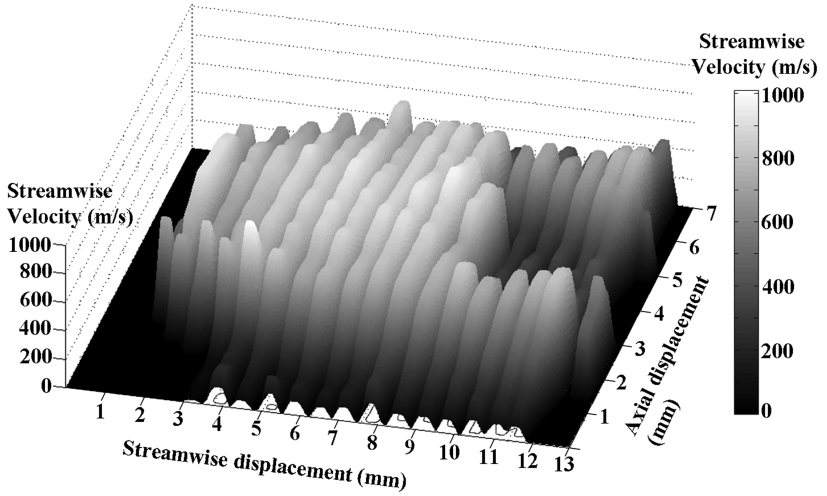

Fig. 8 Resulting streamwise velocity map from addition of velocity maps for all measurement locations.

resolution was 1×1 mm in the field of view. The average streamwise velocity map was similar to the integrated images at the same location. The root mean squared streamwise velocity map showed 1σ uncertainties of 40–60 m/s throughout the flowfield, corresponding to an relative error of about 5% for average streamwise velocities of 800 m/s. The uncertainties were lowest in areas of highest signal-to-noise ratio (for higher number densities, found in the barrel shock area) and slightly higher in areas of lower signal-to-noise ratio (for lower number densities, found in the isentropic expansion area). Overall, the low uncertainties for the single-shot analysis are promising for application of this technique toward single-shot facilities such as shock tubes, or for statistical analysis in dynamic flowfields. The uncertainties could be reduced further with higher signal to noise. This could be accomplished with a higher seeding NO_2 density followed by higher photodissociation laser intensity (through using lenses to focus the laser beam and/or by increasing the overall laser power) because the fraction of NO_2 photodissociated was >99.9%. In addition, the razor blades defining the photodissociation line could be placed closer to the flowfield, which would provide sharper lines and more precise location of the edges. Longer time delays could also be employed to produce more accurate velocity maps. However, this would result in lower spatial resolution as the velocity measurements become more averaged. We also examined the effect of diffusion as a potential source of systematic errors in the edge-finding procedures. In the limit of isotropic diffusion, there was no effect other than a decrease in the intensity of the gradient, which may become an issue in the case of closely spaced beams in a gridded application of MTV or in noisy images. In the presence of strong density gradients, such as those encountered across the Mach disk, diffusion may not be isotropic, and thus may lead to uncertainties in the calculated velocities due to edge-finding inaccuracies. Additional decreases in uncertainty could be achieved by fitting a distribution (such as a Gaussian distribution) to the profile of the tagged flow.

As an additional note, this experiment demonstrated the advantage of probing $NO_{v=1}$ in the underexpanded jet flowfield. However, this flowfield possesses relatively low temperatures (320 K and below), and so it would be useful to examine the application of such a technique in higher temperature flowfields, such as combustion flowfields, which would contain naturally produced NO; this NO would then cause NO background fluorescence which would decrease the contrast of MTV images and cause higher uncertainties in the derived velocity maps. Given the Boltzmann fractions of $NO_{v=1}$ and $NO_{v=0}$ occurring at high temperatures, probing $NO_{v=1}$ rather than $NO_{v=0}$ through seeded NO_2 photodissociation should be advantageous over a wide range of temperatures. However, an important caveat is that, at elevated temperatures, not all of the seeded NO_2 would be available for photodissociation. In fact, the thermal decomposition of NO_2 at elevated temperatures must be considered, as this will decrease the amount of NO_2 surviving for photodissociation, and would lower the signal enhancement for probing either $NO_{v=0}$ or $NO_{v=1}$. For example, studies conducted in [20] reported an 80% loss of NO_2 seeded at 5% due to thermal decomposition in a laminar premixed ethylene–air flame. At these conditions, the signal enhancement (defined as the $NO_{v=0}$ or $NO_{v=1}$ photodissociation signal assuming saturated photodissociation signal, divided by signal from background $NO_{v=0}$ or $NO_{v=1}$) for probing $NO_{v=1}$ would drop below unity, but the signal enhancement for $NO_{v=1}$ would still be greater than that of $NO_{v=0}$. Therefore, velocimetry under these conditions is still possible.

B. Integrated and Single-Shot Images for Vibrational Temperature Mapping

To calculate the vibrational temperature from each pair of images ($NO_{v=1}$ and $NO_{v=0}$ probe lasers) at each nominal delay, an image processing code was developed based on extraction of vibrational temperature by assuming a Boltzmann distribution of the two states. The image processing included standard procedures for warping both images to equivalent fields of view, background image subtraction, and laser sheet inhomogeneity correction. The calibration constant was calculated by setting the temperature at the time of photodissociation to the well-known ratio of $NO_{v=1}$:$NO_{v=0}$ formed during photodissociation of NO_2 [12–14]. In this way, differences in average laser intensities and camera sensitivities could be easily calibrated using a single scaling factor. Because each of the integrated images used for the analysis were 300 shot integrations, the shot-to-shot variations in laser intensity did not contribute significantly toward changing the value of the scaling factor. A representative vibrational temperature map taken at 6 μs time delay is shown in Fig. 9. In this figure, the different vibrational relaxation rates associated with the ambient, outer jet, and centerline regions are clear. There is an artificial increase in vibrational temperature near the edges of the tagged line, which originates from low signal to noise in these areas and should be disregarded. In addition, a slight decrease in vibrational temperature toward the downstream portion of the tagged line may be due to the slight time delay (150 ns) between the probing of the $NO_{v=1}$ and $NO_{v=0}$, which was required to allow for the fluorescence from the $NO_{v=1}$ to decay before probing the $NO_{v=0}$, and this temporal delay would produce a slightly colder temperature on the downstream edge. However, these effects would be insignificant and the center of the tagged line represents the true vibrational temperature measurement.

As expected, the outer jets (the areas of highest pressure) experienced the fastest vibrational temperature decay, which are depicted in the figure as the areas with the lowest vibrational temperature. The centerline and ambient regions, at moderate and low pressures, experienced moderate and slow decays resulting in moderate and high vibrational temperatures, respectively. The slight curvature of the vibrational temperature along the edges of the beam is due to low signal to noise in those regions producing artificially high vibrational temperatures and should be disregarded. The centerline profile was modeled using a kinetics model [32] which included both vibration–vibration (V–V) and vibration–translation (V–T) exchanges between all flow species, as well as chemical reactions. The species considered in the kinetics model included ground and first excited vibrational states of NO, O_2, and N_2. Concentrations of chemical species NO_2, O_3, and O were also considered. Rate constants for the relevant reactions were taken from the literature [17,33–41] and reverse rate constants that were not found in the literature were calculate via the principle of detailed balance. The experimental NO T_{vib} (points) and simulated NO T_{vib} (solid line) are presented in Fig. 10.

Because the fit of simulated to experimental data was quite good, sensitivity analyses were conducted on the kinetics model $NO_{v=1}$ to explore the mechanisms which drove the vibrational relaxation of NO. The analyses revealed that the vibrational temperature decay was extremely sensitive throughout the simulation run time to vibrational relaxation of $NO_{v=1}$ by O atoms produced via photo-

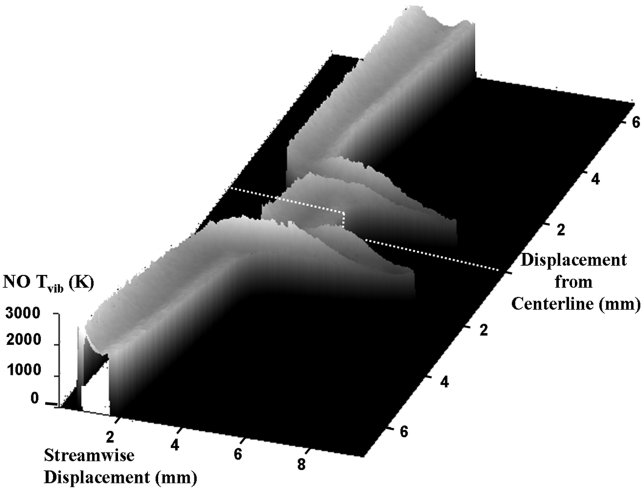

Fig. 9 Typical NO vibrational temperature map at nominal delay of 6 μs.

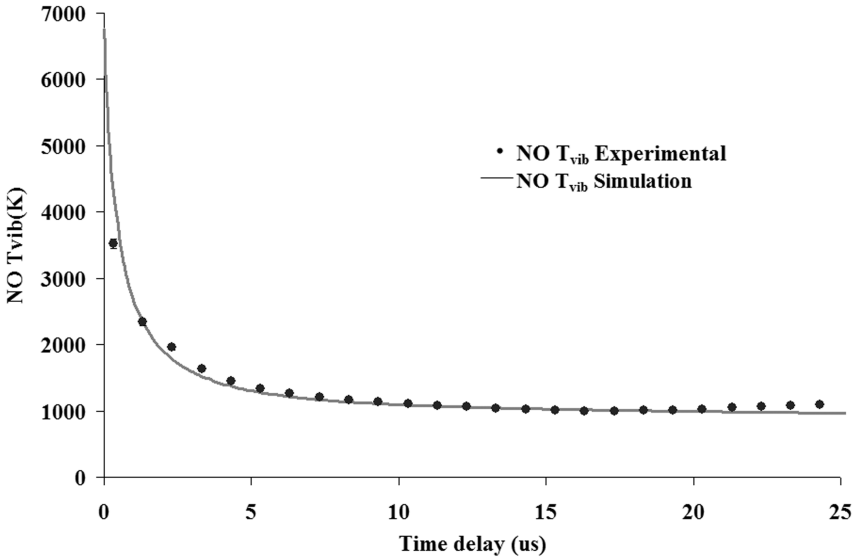

Fig. 10 Experimental and simulated NO vibrational temperature decay along centerline region.

dissociation. At later times (100–200 μs), population depletion of $NO_{v=1}$ became more sensitive to recombination and chemical feed reactions. However, the sensitivity to vibrational relaxation by O atoms was always several times greater, meaning that the reaction was several times more important than those of the nearest competitors, V–V and V–T energy exchanges with O_2. Error analyses involving multiple (40) single-shot pairs of images taken at each of the nominal delays of 0, 5, 10, 15, 20, 25, and 30 μs demonstrated vibrational temperature uncertainties of approximately 6%. This uncertainty includes laser shot-to-shot fluctuations, which were not corrected on an image-by-image basis.

IV. Conclusions

We have conducted studies using the photodissociation of NO_2 and probing the formed NO for measurements of velocity and vibrational temperature in an underexpanded jet. Although other authors have used the photodissociation of NO_2 and subsequent probing of $NO_{v=0}$ for single-component velocimetry, we focused our studies on demonstrating the advantages of probing $NO_{v=1}$ rather than $NO_{v=0}$, particularly for flowfields with naturally occurring NO that would lead to background $NO_{v=0}$ fluorescence. Probing $NO_{v=1}$ in such flowfields would provide higher contrast in the fluorescence images and thus better signal to noise than probing $NO_{v=0}$. These efforts represent the first known study to address the use of probing $NO_{v=1}$ for single-component velocity mapping via molecular tagging velocimetry. This was true for all temperatures within the underexpanded jet (320 K and below) and would also be true at higher temperatures, although, at higher temperatures, the thermal decomposition of NO_2 must be considered. For the velocimetry calculations, a single photodissociation line was employed and measurements were made at multiple downstream positions in the flowfield. The results recovered the expected streamwise velocity map of the underexpanded jet flowfield, with single-shot 1σ uncertainties of 5%.

The vibrational temperature experiments explored the mechanism of $NO_{v=1}$ vibrational decay using kinetics modeling in support of an AFOSR MURI project. The main mechanism for NO vibrational relaxation was collisional quenching with the photolytic O atoms. Error analysis using single-shot PLIF images produced vibrational temperature 1σ uncertainties of about 6%.

We note that the present diagnostic technique could be extended to photodissociate a grid, rather than a single line of NO_2, with subsequent probing of the photodissociated $NO_{v=1}$ to give two components of velocity. Work in such studies is currently underway.

Acknowledgments

The authors wish to acknowledge the contributions from Jacob Dean and Rodrigo Sanchez-Gonzalez as well as contributions from Texas A&M University Chemistry Machine Shop and Oran Nicks Low Speed Wind Tunnel staff. Funding for this research was provided by the U.S. Air Force Office of Scientific Research contract number FA9550-04-1-0425 (John Schmisseur, Program Manager) and Sandia National Labs (Combustion Research Facility).

References

[1] Huffman, R., and Elliott, G., "An Experimental Investigation of Accurate Particle Tracking in Supersonic, Rarefied Axisymmetric Jets," AIAA Paper 2009-1265, 2009.

[2] Pitz, R. W., Brown, T. M., Nandula, S. P., Skaggs, P. A., DeBarber, P. A., Brown, M. S., and Segall, J., "Unseeded Velocity Measurement by Ozone Tagging Velocimetry," *Optics Letters*, Vol. 21, No. 10, 1996, pp. 755–757. doi:10.1364/OL.21.000755

[3] Ribarov, L. A., Wehrmeyer, J. A., Hu, S., and Pitz, R. W., "Multiline Hydroxyl Tagging Velocimetry Measurements in Reacting and Nonreacting Experimental Flows," *Experiments in Fluids*, Vol. 37, No. 1, 2004, pp. 65–74.

[4] Pitz, R. W., Lahr, M. D., Douglas, Z. W., Wehrmeyer, J. A., Hu, S., Carter, C. D., Hsu, K. Y., Lum, C., and Koochesfahani, M. M., "Hydroxyl Tagging Velocimetry in a Mach 2 Flow with a Wall Cavity," AIAA Paper 2005-36, 2005.

[5] Wehrmeyer, J. A., Ribarov, L. A., Oguss, D. A., and Pitz, R. W., "Flame Flow Tagging Velocimetry with 193-nm H_2O Photodissociation," *Applied Optics*, Vol. 38, No. 33, 1999, pp. 6912–6917. doi:10.1364/AO.38.006912

[6] Miles, R., Zhou, D., Zhang, B., and Lempert, W., "Fundamental Turbulence Measurements by Relief Flow Tagging," *AIAA Journal*, Vol. 31, No. 3, 1993, pp. 447–452. doi:10.2514/3.11350

[7] Danehy, P., O'Byrne, S., Houwing, F., Fox, J., and Smith, D., "Flow-Tagging Velocimetry for Hypersonic Flows Using Fluorescence of Nitric Oxide," *AIAA Journal*, Vol. 41, No. 2, 2003, pp. 263–271. doi:10.2514/2.1939

[8] van der Laan, W. P. N., Tolboom, R. A. L., Dam, N. J., and ter Meulen, J. J., "Molecular Tagging Velocimetry in the Wake of an Object in Supersonic Flow," *Experiments in Fluids*, Vol. 34, No. 4, 2003, pp. 531–533.

[9] Nandula, S. P., Pitz, R. W., Bominaar, J., Schoemaecker, C., Dam, N. J., and ter Meulen, J. J., "Kinetics of NO Tag Formation in Air for Unseeded Molecular Tagging Velocimetry," AIAA Paper 2004-390, 2004.

[10] Nakaya, S., Kasahara, M., Tsue, M., and Kono, M., "Velocity Measurements of Reactive and Non-reactive Flows by NO-LIF Method

Using NO_2 Photodissociation," *Heat Transfer, Asian Research*, Vol. 34, No. 1, 2005, pp. 40–52.
doi:10.1002/htj.20038

[11] Orlemann, C., Schulz, C., and Wolfrum, J., "NO-Flow Tagging by Photodissociation of NO_2. A New Approach for Measuring Small-Scale Flow Structures," *Chemical Physics Letters*, Vol. 307, Nos. 1–2, 1999, pp. 15–20.
doi:10.1016/S0009-2614(99)00512-6

[12] Hunter, M., Reid, S. A., Robie, D. C., and Reisler, H., "The Monoenergetic Unimolecular Reaction of Expansion-Cooled NO_2:NO Product State Distributions at Excess Energies 0–3000 cm^{-1}," *Journal of Chemical Physics*, Vol. 99, No. 2, 1993, pp. 1093–1108.
doi:10.1063/1.465408

[13] Brooks, C., Hancock, G., and Saunders, M., "Dependence of the Nascent Vibrational Distribution of NO(v) on the Photolysis Wavelength of NO_2 in the Range $\lambda = 266$–327 nm Measured by Time-Resolved Fourier Transform Infrared Emission," *Physical Chemistry Chemical Physics*, Vol. 9, No. 38, 2007, pp. 5232–5240.
doi:10.1039/b710594k

[14] Harrison, J., Yang, X., Rosslein, M., Felder, P., and Huber, J., "Photodissociation of NO_2 at 355 and 351 nm Investigated by Photofragment Translational Spectroscopy," *Journal of Physical Chemistry*, Vol. 98, No. 47, 1994, pp. 12260–12269.
doi:10.1021/j100098a023

[15] Cheng, H., and Emanuel, G., "Perspective on Hypersonic Nonequilibrium Flow," *AIAA Journal*, Vol. 33, No. 3, 1995, pp. 385–400.
doi:10.2514/3.12446

[16] Scalabrin, L., and Boyd, I., "Development of an Unstructured Navier–Stokes Solver for Hypersonic Nonequilibrium Aerothermodynamics," AIAA Paper 2005-5203, 2005.

[17] Candler, G., "Translation-Vibration-Dissociation Coupling in Nonequilibrium Hypersonic Flows," AIAA Paper 89-1739, 1989.

[18] Osipov, A., Uvarov, A., and Vinnichenko, N., "Influence of the Initial Vibrationally Non-Equilibrium State of a Medium on the Structure of Von Karman Vortex Sheet," *Physics of Fluids*, Vol. 18, No. 10, 2006, pp. 105106.1–7.
doi:10.1063/1.2364261.

[19] Roy, C., and Blottner, F., "Review and Assessment of Turbulence Models for Hypersonic Flows: 2D/Axisymmetric Cases," AIAA Paper 2006-713, 2006.

[20] Menon, A., Lee, S., Linevsky, M., Litzinger, T., and Santoro, R., "Addition of NO_2 to a Laminar Premixed Ethylene-Air Flame: Effect on Soot Formation," *Proceedings of the Combustion Institute*, Vol. 31, No. 1, 2007, pp. 593–601.
doi:10.1016/j.proci.2006.08.105

[21] McMillin, B., Lee, M., and Hanson, R., "Planar Laser-Induced Fluorescence Imaging of Nitric Oxide in Shock Tube Flows with Vibrational Nonequilibrium," AIAA Paper 90-1519, 1990.

[22] Eckbreth, A., *Laser Diagnostics for Combustion Temperature and Species*, Abacus, Cambridge, MA, 1988.

[23] Nee, J., Juan, C., Hsu, J., Yang, J., and Chen, W., "The Electronic Quenching Rates of NO $A^2\Sigma^+$, $v' = 0$–2," *Chemical Physics*, Vol. 300, Nos. 1–3, 2004, pp. 85–92.
doi:10.1016/j.chemphys.2004.01.014

[24] Woodmansee, M. A., Iyer, V., Dutton, J. C., and Lucht, R. P., "Nonintrusive Pressure and Temperature Measurements in an Underexpanded Sonic Jet Flowfield," *AIAA Journal*, Vol. 42, No. 6, 2004, pp. 1170–1180.
doi:10.2514/1.10418

[25] Donaldson, C. D., and Snedeker, R. S., "A Study of Free Jet Impingement. Part 1: Mean Properties of Free and Impinging Jets," *Journal of Fluid Mechanics*, Vol. 45, No. 2, 1971, pp. 281–319.
doi:10.1017/S0022112071000053

[26] Wilkes, J. A., Glass, C. E., Danehy, P. M., and Nowak, R. J., "Fluorescence Imaging of Underexpanded Jets and Comparison with CFD," AIAA Paper 2006-910, 2006.

[27] Wilkes, J. A., Danehy, P. M., and Nowak, R. J., "Fluorescence Imaging Study of Transition in Underexpanded Free Jets," NASA TR-20050232745, 2005.

[28] Palmer, J. L., McMillin, B. K., and Hanson, R. K., "Planar Laser-Induced Fluorescence Imaging of Underexpanded Free Jet Flow in a Shock Tunnel Facility," AIAA Paper 91-1687, 1991.

[29] Kulatilaka, W. D., Naik, S. V., and Lucht, R. P., "Development of High-Spectral-Resolution Planar Laser-Induced Fluorescence Imaging Diagnostics for High-Speed Gas Flows," *AIAA Journal*, Vol. 46, No. 1, 2008, pp. 17–20.
doi:10.2514/1.34971

[30] Luque, J., and Crosley, D. R., "LIFBASE: Database and Spectral Simulation Program (Version 1.5)," SRI International Rept. MP 99-009, 1999.

[31] Hsu, A., "Application of Advanced Laser and Optical Diagnostics Towards Non-Thermochemical Equilibrium Systems," Ph.D. Dissertation, Texas A&M Univ., College Station, TX, 2009.

[32] Ianni, J., Kintecus, Windows XP Ver., 2008, www.Kintecus.com.

[33] Kosanetzky, J., List, U., Urban, W., Vormann, H., and Fink, E. H., "Vibrational Relaxation of NO ($X^2\Pi$, $v = 1$) Studied by an IR-UV-Double-Resonance Technique," *Chemical Physics*, Vol. 50, No. 3, 1980, pp. 361–371.
doi:10.1016/0301-0104(80)85106-8

[34] Bohm, B., Doughty, A., Hancock, G., Moore, E., and Morrell, C., "Vibrational Relaxation of NO($v = 1$–3) and NO_2 (0,0,1) with Atmospheric Gases," *Physical Chemistry Chemical Physics*, Vol. 1, No. 8, 1999, pp. 1833–1842.
doi:10.1039/a809995b

[35] Green, B., Caledonia, G., Murphy, R., and Robert, F., "The Vibrational Relaxation of NO($v = 1$–7) by O_2," *Journal of Chemical Physics*, Vol. 76, No. 5, 1982, pp. 2441–2448.
doi:10.1063/1.443273

[36] Dodd, J., Lockwood, R., Hwang, E., Miller, S., and Lipson, S., "Vibrational Relaxation of NO($v = 1$) by Oxygen Atoms," *Journal of Chemical Physics*, Vol. 111, No. 8, 1999, pp. 3498–3507.
doi:10.1063/1.479671

[37] Ahn, T., Adamovich, I., and Lempert, W., "Determination of Nitrogen *V-V* Transfer Rates by Stimulated Raman Pumping," *Chemical Physics*, Vol. 298, Nos. 1–3, 2004, pp. 233–240.
doi:10.1016/j.chemphys.2003.11.029

[38] Johnbaik, R., "Theoretical Investigation of the Vibrational Relaxation of Nitric Oxide ($n = 1$–7) in Collisions with O_2 and N_2," *Bulletin of the Korean Chemical Society*, Vol. 14, No. 1, 1993, pp. 47–52.

[39] Demore, W., Sander, S., Golden, D., Hampson, R., Kurylo, M., Howard, C., Ravishankara, A., Kolb, C., and Molina, M., "Chemical Kinetics and Photochemical Data for Use in Stratospheric Modeling," Jet Propulsion Lab., California Inst. of Technology Paper 97-4, 1997.

[40] Atkinson, R., Baulch, D., Cox, R., Crowley, J., Hampson, R., Hynes, R., Jenkin, M., Rossi, M., and Troe, J., "Evaluated Kinetic and Photochemical Data for Atmospheric Chemistry, Volume I: Gas Phase Reactions of O_x, HO_x, NO_x and SO_x Species," *Atmospheric Chemistry and Physics*, Vol. 4, No. 6, 2004, pp. 1461-1738.

[41] Tsang, W., and Hampson, R., "Chemical Kinetic Database for Combustion Chemistry, Part 1: Methane and Related Compounds," *Journal of Physical and Chemical Reference Data*, Vol. 15, No. 3, 1986, pp. 1087–1279.

N. Chokani
Associate Editor